Check for updates

Advanced Functional Materials

ADVANCED FUNCTIONAL MATERIALS
www.afm-journal.de

RESEARCH ARTICLE

Ultra-Sensitive Reconfigurable SERS Platform Enabled by Tunable Plasmonic Nanogaps

Jiaye Du[1] | Ruirui Ren[1] | Fengguang Shen[1] | Jiajun Li[3] | Leilei Hou[1] | Jingjing Wei[1] | Xiuying Liu[1] | Ming Kang[1] | Lei Zhou[2] | Feifei Liu[1]

[1]College Physics & Materials Science, Tianjin Normal University, Tianjin, People's Republic of China | [2]State Key Laboratory of Surface Physics, Shanghai Key Laboratory of Metasurfaces for Light Manipulation and Department of Physics, Fudan University, Shanghai, People's Republic of China | [3]Material Science and Engineering, Physical Science Engineering (PSE) Division, King Abdullah University of Science and Technology, Thuwal, Saudi Arabia

Correspondence: Lei Zhou (phzhou@fudan.edu.cn) | Feifei Liu (liufeifei@tjnu.edu.cn)

Received: 6 September 2026 | **Revised:** 9 October 2026 | **Accepted:** 29 October 2026

Keywords: detection versatility | SERS sensor | silver nanoparticles | single-molecule sensitivity | stepwise nanogap modulation

ABSTRACT

Plasmonic nanogaps that generate intense electromagnetic hot spots are crucial for surface-enhanced Raman scattering (SERS) sensing, particularly at the single-molecule level. However, plasmonic nanogaps in conventional SERS platforms are usually fixed, posing significant challenges for precise and ultra-sensitive molecular detection. Here, we propose a stretchable SERS platform, on which plasmonic nanogaps can be modulated stepwise, to sequentially control the trapping and deposition of target molecules, which are subsequently detected by significantly enhanced Raman signals. Functionalized with monodisperse silver nanoparticles, the platform enables reversible and precise bidirectional tuning of plasmonic nanogaps from nearly 400 nm down to sub-5 nm, endowing the SERS sensor with excellent sensitivity, robust reconfigurability, and broad detection versatility. SERS measurements on various small-molecule analytes achieve the lowest detectable concentrations of 10^{-14} M (rhodamine 6G, R6G), 10^{-12} M (4-Mercaptopyridine, 4-MPY), and 10^{-5} M (urea and sodium lactate). The dual-analyte measurement confirms the single-molecule SERS detection capability. Meanwhile, large biomolecules (hemoglobin, Hb) detection down to a limit of 10 pg/mL further validates the reliability and universality of the developed SERS sensor. Our scheme paves the road for ultrasensitive detection of arbitrary molecules with robust reconfigurability.

1 | Introduction

Surface-enhanced Raman scattering (SERS) is a label-free and high-sensitivity molecular fingerprinting detection technique [1–4]. It has been reported that more than 50% of SERS signals derive from nanoscale interstices or gaps formed between metallic structures [5], which support localized surface plasmon resonances (LSPRs) [6–9]. Narrower plasmonic nanogaps produce stronger localized electromagnetic fields and higher SERS enhancement. Nevertheless, reduced gap sizes substantially decrease the probability of analyte molecules accessing the target electromagnetic hotspots [10–12]. An inherent trade-off therefore exists between nanogap dimension and molecular accessibility. This imposes critical challenges, especially for single-molecule SERS detection, manifested mainly in sensitivity, reproducibility, and detection efficiency of the sensor [13–17].

Flexible SERS platforms featuring tunable nanogaps offer a novel strategy to improve molecular loading efficiency and SERS detection sensitivity [18–21]. Meanwhile, they enable conformal sampling on arbitrary surfaces, making them suitable for in situ and on-site detection [19–22]. According to distinct substrate modulation strategies, flexible SERS substrates can be mainly classified into two categories: stretchable and

All rights reserved, including rights for text and data mining and training of artificial intelligence technologies or similar technologies.
© 2026 Wiley-VCH GmbH

bendable polymer substrates regulated by mechanical [23, 24] or thermal stimuli [25], and swellable substrates based on hydrogels [26, 27] or filter papers [28] that are modulated through water absorption and desorption. Nanostructures on stretchable flexible substrates are conventionally prepared under strain-free conditions, and post-stretching of the substrate only enables tunable expansion of nanogaps [29, 30]. Therefore, to achieve high-sensitivity SERS detection, nanostructures with sub-nanometer gaps usually need to be preconstructed, which imposes stringent demands on micro/nanofabrication techniques [31, 32]. Hydrogel substrates can stably support nanoassembled structures via their tunable hydrated intermediate state, thus allowing bidirectional nanogap regulation involving both expansion and contraction [26, 33–35]. However, hydrogel platforms generally suffer from a relatively low regulation speed. Furthermore, the intrinsic 3D cross-linked network structure limits their compatibility with diverse analytes, ranging from small molecules to large biomolecules [35]. Paper-based substrates possess natural porosity and a high concentration of hydroxyl-type hydrophilic groups, which facilitates metal deposition without the need for extensive processing [28, 36]. Nevertheless, they are susceptible to moisture absorption and deformation, and exhibit relatively low precision in plasmonic nanogap regulation [18].

Herein, we propose an innovative and precise plasmonic nanogap modulation strategy for stretchable platforms, enabling sequential manipulation of nanogap expansion and contraction with rapid response and low operational cost. The stretchable substrate is decorated with randomly dispersed silver nanoparticles. Upon uniaxial stretching, the stretchable substrate exhibits opposite nanogap-modulation behaviors along two orthogonal directions (see Figure 1a, where the nanogap size g_1 increases while g_2 decreases). Accordingly, two-step orthogonal stretching of the flexible substrates allows reversible bidirectional nanogap tuning (expansion and contraction) at a single spatial position (see yellow dotted circles in insets 1–4 of Figure 1b). Experimental results show that nanogaps among monodisperse silver nanoparticles are precisely tunable from nearly 400 nm to sub-5 nm. This unique feature sequentially promotes molecular trapping, deposition (insets 1–3 of Figure 1b), and Raman enhancement (inset 4 of Figure 1b). SERS measurements for diverse analytes, including small molecules (R6G, 4-MPY, urea and sodium lactate) and large biomolecules (hemoglobin, Hb) yield ultralow limits of detection, demonstrating the excellent universality and robust reliability of the proposed platform. Moreover, dual-analyte characterization further verifies the superior single-molecule detection capability of the SERS sensor.

2 | Results and Discussion

2.1 | Dynamic Tuning of Plasmonic Nanogaps Under Tensile Strain

Vacuum thermal evaporation was employed to directly deposit silver nanoparticles onto thermally stable modified Polydimethylsiloxane (PDMS) film, with nanoparticle deposition time and evaporation rate as the primary optimized parameters in the experiment. A dense monolayer of nanoparticles with different sizes is randomly distributed on the surface of the flexible substrate (see scanning electron microscope (SEM) images in Figure S1). PDMS is a crosslinked elastomer. Under appropriate external stress, the curled siloxane backbone network inside the material undergoes directional stretching, leading to elongation of the substrate along the tensile direction and transverse contraction perpendicular to the tensile direction [37, 38]. Such mechanical deformation of the substrate can drive the expansion or compression of the gaps between silver nanoparticles on its surface. To clarify the strain-dependent evolution of nanogaps in the randomly dispersed nanoparticles, we employed a membrane transfer method to immobilize and replicate the nanostructures at varied tensile strains, where tensile strain is defined as $\xi = \Delta l/l_0$, with l_0 and Δl denoting the initial length and the elongation of the PDMS substrate, respectively. As illuminated in Figure 2a, Polyurethane (PU) solution is directly coated on the pre-stretched and Ag nanoparticle-decorated PDMS substrate. Following natural air drying, the PU layer is peeled off from the PDMS surface, enabling the transfer of nanoparticles onto the flexible PU film. The fourth inset of Figure 2a shows the optical photographs of the PDMS substrate after partial nanostructure exfoliation and the corresponding PU film loaded with transferred Ag nanoparticles. Complete stripping of nanoparticles from the PDMS substrate using the PU film was verified. Therefore, the nanostructures transferred onto the PU film can faithfully reproduce the morphology of those originally formed on the stretched PDMS substrate.

Figure 2b-e show the SEM images of the transferred nanoparticles with $\xi = 0$, 0.23, 0.43 and 0.68, respectively. At zero tensile strain (*i. e.*, $\xi = 0$), nanoparticles are randomly distributed across the substrate surface with relatively uniform interparticle distances, as illustrated in Figure 2b and its enlarged view in Figure 2f. Statistical analysis of approximately 700 nanogap pairs extracted from Figure 2f reveals that nanogaps in the 35–50 nm range constitute the dominant fraction (see Figure 2j). As tensile strain increases, stripe-shaped nanogaps between nanoparticles emerge and gradually broaden along the stretching direction (outlined by the white dotted circles in Figure 2c-e). The red histograms in Figure 2k,i statistically analyze the effect of mechanical stretching on the enlargement of nanogaps. It can be observed that as the stretching strain increases, gaps ranging from 100 to 400 nm gradually emerge and their fraction rises continuously in the analyzed regions of Figure 2g,h, respectively. Such reversibly expanded interparticle channels promote efficient molecular deposition. Nevertheless, inhomogeneous tensile stress at microscopic interfaces prevents perfect uniaxial alignment of the strip-shaped nanogaps. Such structural disorder is significantly aggravated at a tensile strain of $\xi = 0.68$ (see Figure 2e), where Zig-zag striped interparticle gaps form between the nanoparticles. Figure S2 summarizes the evolution of nanogaps in the directions parallel and perpendicular to the stretching axis. The fraction of nanogaps in the 100–400 nm is markedly higher along the stretching direction. Notably, apart from stretch-induced striped nanogaps, tensile deformation also drastically reduces interparticle gaps, especially along the direction perpendicular to the stretching axis. As the tensile strain increases from $\xi = 0.23$ to 0.43, the predominant nanogap size decreases from 20–30 to 5–10 nm (see the blue histograms in Figure 2k,i), in which nanogaps with sizes below 5 nm account for 7–16% of the total population. However, when the tensile strain reaches 0.68, the nanoparticles within

16163028, 0, Downloaded from https://advanced.onlinelibrary.wiley.com/doi/10.1002/adfm.79500 by Fudan University, Wiley Online Library on [10/11/2026]. See the Terms and Conditions (https://onlinelibrary.wiley.com/terms-and-conditions) on Wiley Online Library for rules of use; OA articles are governed by the applicable Creative Commons License

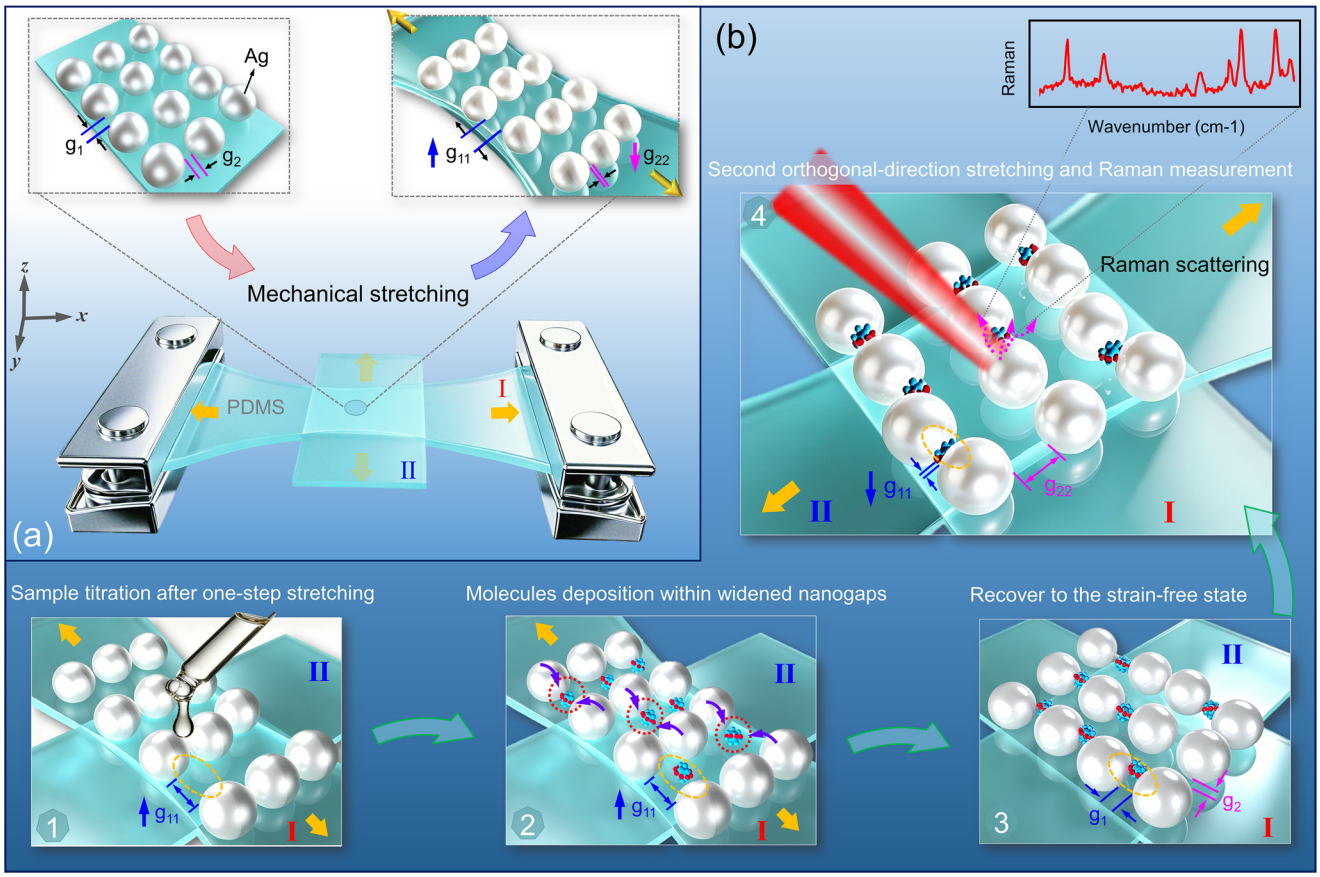


FIGURE 1 | Schematic illustration of the principle and realization of the stepwise nanogap modulation strategy. (a) Regulatory effect of single-step stretching on plasmonic nanogaps; (b) Schematic diagram of the stepwise plasmon nanogap modulation strategy to sequentially control molecular trapping, deposition, and Raman enhancement via a stretchable SERS platform.

numerous domains suffer severe agglomeration, as observed in Figure 2e and its enlarged view in Figure 2i.

Strain-induced modulation on the nanostructured system manifests not only in the above-mentioned microscopic morphology but also in its optical spectroscopic responses. Accordingly, we performed both numerical simulations and in situ absorption spectrum characterizations on the PDMS-based SERS substrates under different tensile strains. Figure 3a presents the statistical diameter distribution of nanoparticles on the strain-free substrate shown in Figure 2f), where nanoparticles with an average diameter of ~130 nm constitute the major population; the purple solid curve is the fitting result. Using this measured mean nanoparticle diameter, we simulated the absorption spectra of nanoparticle dimers featuring different interparticle nanogap widths d, as plotted in Figure 3b, where the nanogap widths d change at unequal intervals from 80 to 1 nm. In all simulations, incident light is linearly polarized parallel to the nanogap, as illuminated in Figure 3c. For relatively large nanogaps ranging from 80 to 30 nm, the resonant wavelengths of the broadband absorption peaks for Ag dimers remain almost unchanged, as indicated by the purple and blue curves in Figure 3b. In contrast, a prominent redshift occurs in the absorption spectra when the nanogap width d shrinks below 10 nm, corresponding to the green and red curves in Figure 3b. The physical mechanism behind such spectral evolution can be verified by the near-field electric intensity distributions of nanoparticle dimers with d = 80 and 5 nm, respectively, as illustrated in Figure 3c. It can be observed that the spectral responses for the dimers with relatively large nanogaps (e.g., d = 80 nm), originate mainly from the electric dipole resonance of individual nanoparticles, while those separated by a 5 nm interparticle gap arise from the so-called gap plasmon resonance, due to strong near-field coupling between nanoparticles [39, 40]. Compared with the electric field intensity distribution of dipole resonance, the gap plasmonic mode within nanogaps generates a nearly 70-fold local electric-field enhancement relative to the dipole-resonant field. Correspondingly, the molecular Raman signal within hot spots is further enhanced by at least 10^3-fold with respect to the substrate exhibiting only dipole resonance.

In experimental spectroscopic measurements, two orthogonal linear polarization modes of incident light are utilized, as illustrated in Figure 3d: the transverse magnetic (TM) mode, where the electric field vector is orthogonal to the substrate stretching direction, and the transverse electric (TE) mode, with its electric field aligned parallel to the stretching axis. Figure 3e,f shows the in situ measured absorption spectra of SERS substrate for TM and TE polarizations, respectively. The applied tensile strain is tuned from ξ = 0 to 0.7 at an interval of 0.1. The dotted curves in Figure 3e,f correspond to the measurement results, while the solid curves represent the spectral fitting results. The relatively narrow absorption peak centered at λ = 500 nm originates from the intrinsic characteristic signal of a super-continuous white-light

16163028, 0, Downloaded from https://advanced.onlinelibrary.wiley.com/doi/10.1002/adfm.79500 by Fudan University, Wiley Online Library on [10/11/2026]. See the Terms and Conditions (https://onlinelibrary.wiley.com/terms-and-conditions) on Wiley Online Library for rules of use; OA articles are governed by the applicable Creative Commons License

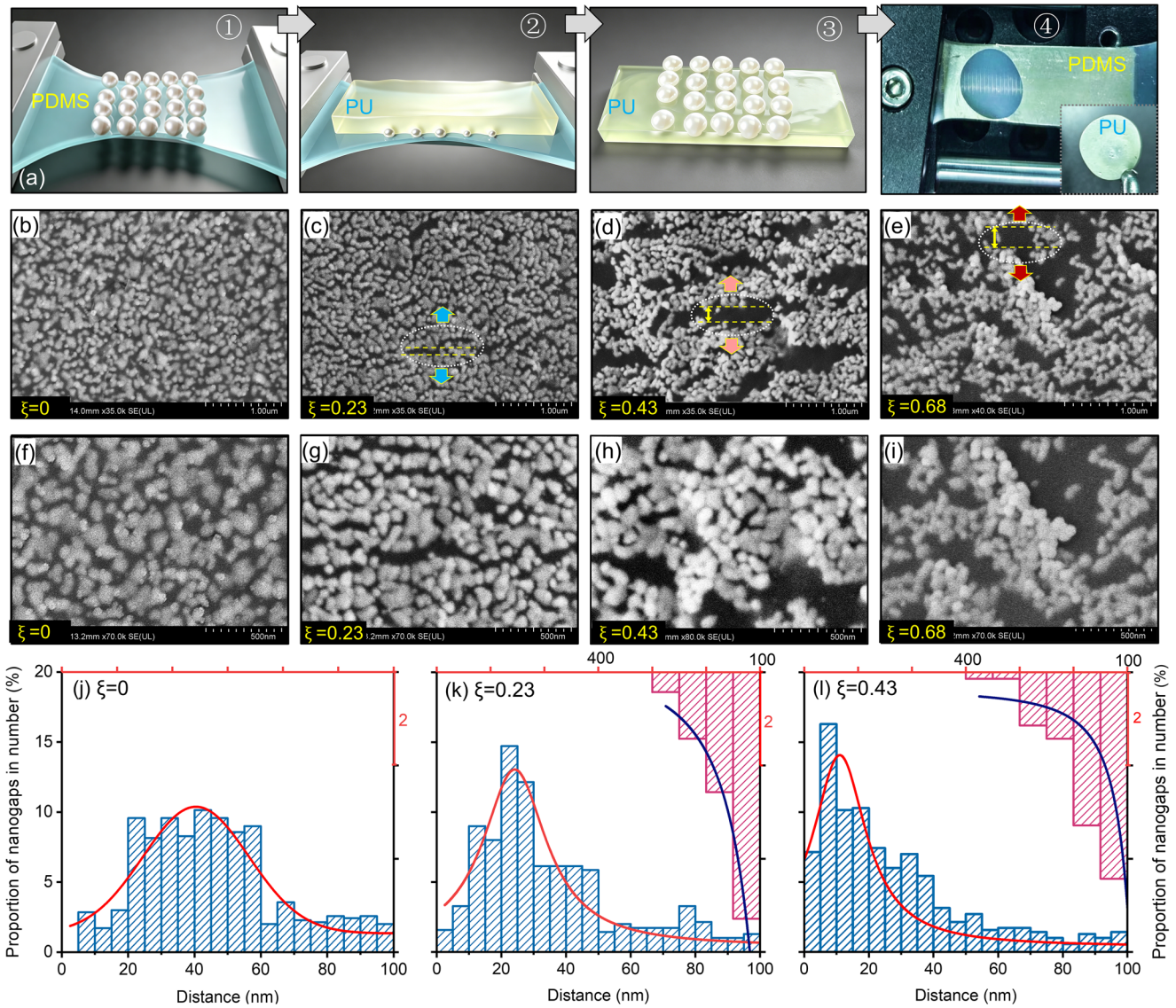


FIGURE 2 | Microscopic distribution of Ag nanoparticles on the surface of a flexible substrate under tensile stretching. (a) Schematic workflow of the peeling-assisted film transfer strategy for replicating Ag nanoparticles (insets 1–3) and the optical photograph of the PDMS substrate after partial nanostructure exfoliation (inset 4); (b)-(e) SEM images of the transferred nanostructures at $\xi = 0$, 0.23, 0.43 and 0.68, respectively; (f)-(i) Corresponding magnified views of panels (b)-(e); (j)-(l) Statistical analysis of nanogap sizes extracted from the images in Figure 2f–h, respectively.

laser source. Under TM polarization, the broadband absorption peaks originating from the LSPR of Ag nanoparticles undergo an obvious redshift from about 400 to 700 nm as the tensile strain ξ increases from 0 to 0.7. This phenomenon reveals the drastic reduction in nanogap width along the direction perpendicular to the stretching axis, which is consistent with the evolution features of nanostructure distribution outlined above. In contrast, only a slight spectral redshift is observed for the plasmonic absorption peaks under TE polarization. The spectral evolution under TE polarization can be mainly attributed to two factors. First, stripe-like nanogaps emerge and gradually broaden along the stretching direction. Such morphological changes barely induce notable spectral variations, since the measured extinction spectra are dominated by the electric dipole resonance of individual nanoparticles, as validated by simulation results. Second, non-uniform deformation of the substrate reduces local nanogaps parallel to the stretching direction, which is responsible for the weak redshift of the absorption peaks.

Overall, both simulated and experimentally measured spectroscopic responses of flexible SERS substrates under different tensile strains agree well with the experimentally observed morphological evolution, fully demonstrating that uniaxial tensile stretching can effectively modulate the nanogap widths along two orthogonal dimensions. More importantly, this understanding motivates a two-step nanogap modulation strategy for improving the comprehensive performance of SERS platforms. Figure 3g presents the TM-polarized absorption spectra of the SERS substrate over ten successive stretch-release cycles, where the tensile strain ξ was varied from 0.2 to 0.5. Repeated stretching induces negligible changes in the extinction spectra of the substrate, verifying its outstanding structural stability.

16163028, 0, Downloaded from https://advanced.onlinelibrary.wiley.com/doi/10.1002/adfm.79500 by Fudan University, Wiley Online Library on [10/11/2026]. See the Terms and Conditions (https://onlinelibrary.wiley.com/terms-and-conditions) on Wiley Online Library for rules of use; OA articles are governed by the applicable Creative Commons License

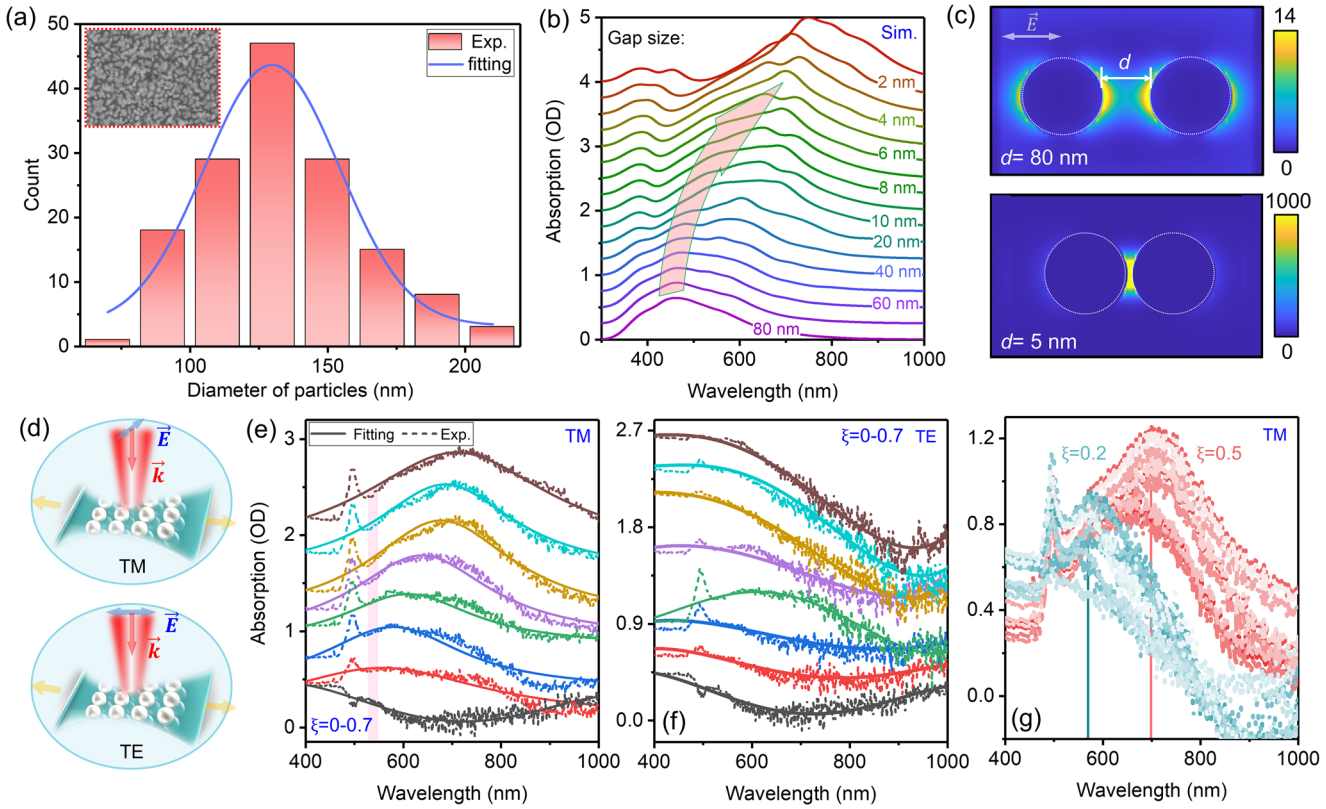


FIGURE 3 | Optical spectral responses of the flexible substrate under tensile stretching. (a) The statistical diameter distribution of nanoparticles on the strain-free substrate shown in Figure 2f; (b) Simulated absorption spectra of nanoparticle dimers featuring different interparticle nanogap widths d, the diameter of nanoparticle is 130 nm; (c) Simulated electric-field intensity distributions of nanoparticle dimer with d = 80 and 5 nm, respectively; (d) Schematic illustration of two orthogonal linearly polarization lights (i.e., TM and TE modes) utilized in experiments; (e) and (f) In situ measured absorption spectra of SERS substrate under stretching, with tensile strain ξ ranging from 0 to 0.7 for TM and TE polarizations, respectively; (g) TM-polarized absorption spectra of the SERS substrate over ten successive stretch-release cycles.

2.2 | Molecular SERS Performance on Strain-Modulated Stretchable Substrates

After verifying the aforementioned fundamental properties, we systematically investigate the SERS performance of analyte molecules adsorbed on the flexible SERS substrate under single uniaxial stretching and two successive orthogonal stretching processes. Figure 4a–c depict the SERS measurement workflows for the flexible substrates subjected to single uniaxial stretching (*single-step-stretching test*) and two successive orthogonal stretching (*two-step-stretching test*). The analyte solution is first titrated onto the pre-stretched substrate, where the nanogaps are broadened to facilitate the adsorption and deposition of target molecules (see Figure 4a). After the analyte solution is fully evaporated and dried, the substrate is relaxed back to its strain-free state for subsequent Raman characterization (see Figure 4b). These procedures constitute the single-step-stretching tests. In contrast, the two-step-stretching SERS measurement refers to the characterization performed during secondary stretching along the axis orthogonal to the initial stretching direction after the substrate recovers to its initial dimension (see Figure 4c and Figure S3). Secondary stretching can effectively narrow the molecule-hosting nanogaps, further enhancing the Raman scattering intensity of molecules and increasing the detection probability of target analytes.

Figure 4d shows the average SERS spectra of 10^{-7} M R6G molecules under single uniaxial stretching conditions, where the flexible SERS substrate is subjected to tensile strains ξ_1 ranging from 0.35 to 0.70. It should be mentioned in here that all SERS spectra are acquired by averaging spatially scanned measurements over a 46 μm × 46 μm mapping area with a scanning step size of 1 μm. Characteristic peaks of R6G at 613, 775, 1187, 1309, 1360 and 1506 cm^{-1} can be clearly resolved in all measured spectra, which are consistent with previous reports [41–44]. Moreover, the Raman peak intensities vary distinctly with the applied tensile strain. Based on triplicate repeated experiments, a well-defined optimal correlation can be observed between the characteristic Raman peak intensity and substrate tensile strain ξ_1, as displayed in Figure 4e,f. These two subfigures depict the intensity evolution of the characteristic peaks at 613 and 775 cm^{-1}, respectively, where the solid red curves correspond to the Gaussian fitting of the experimental data. The maximum Raman signal consistently appears at a tensile strain of $\xi_1 \approx 0.55$. The corresponding average enhancement factor (EF) is calculated to be approximately 10^7 at the 613 cm^{-1} characteristic peak, in comparison with that acquired from a continuous Ag film incubated with 10^{-3} M R6G solution. For further details and supporting data, see the Methods section and Figure S4 [41, 45, 46].

Figure 4g displays the SERS spectra of 10^{-7} M R6G molecules under two successive orthogonal stretching conditions. The

16163028, 0, Downloaded from https://advanced.onlinelibrary.wiley.com/doi/10.1002/adfm.79500 by Fudan University, Wiley Online Library on [10/11/2026]. See the Terms and Conditions (https://onlinelibrary.wiley.com/terms-and-conditions) on Wiley Online Library for rules of use; OA articles are governed by the applicable Creative Commons License

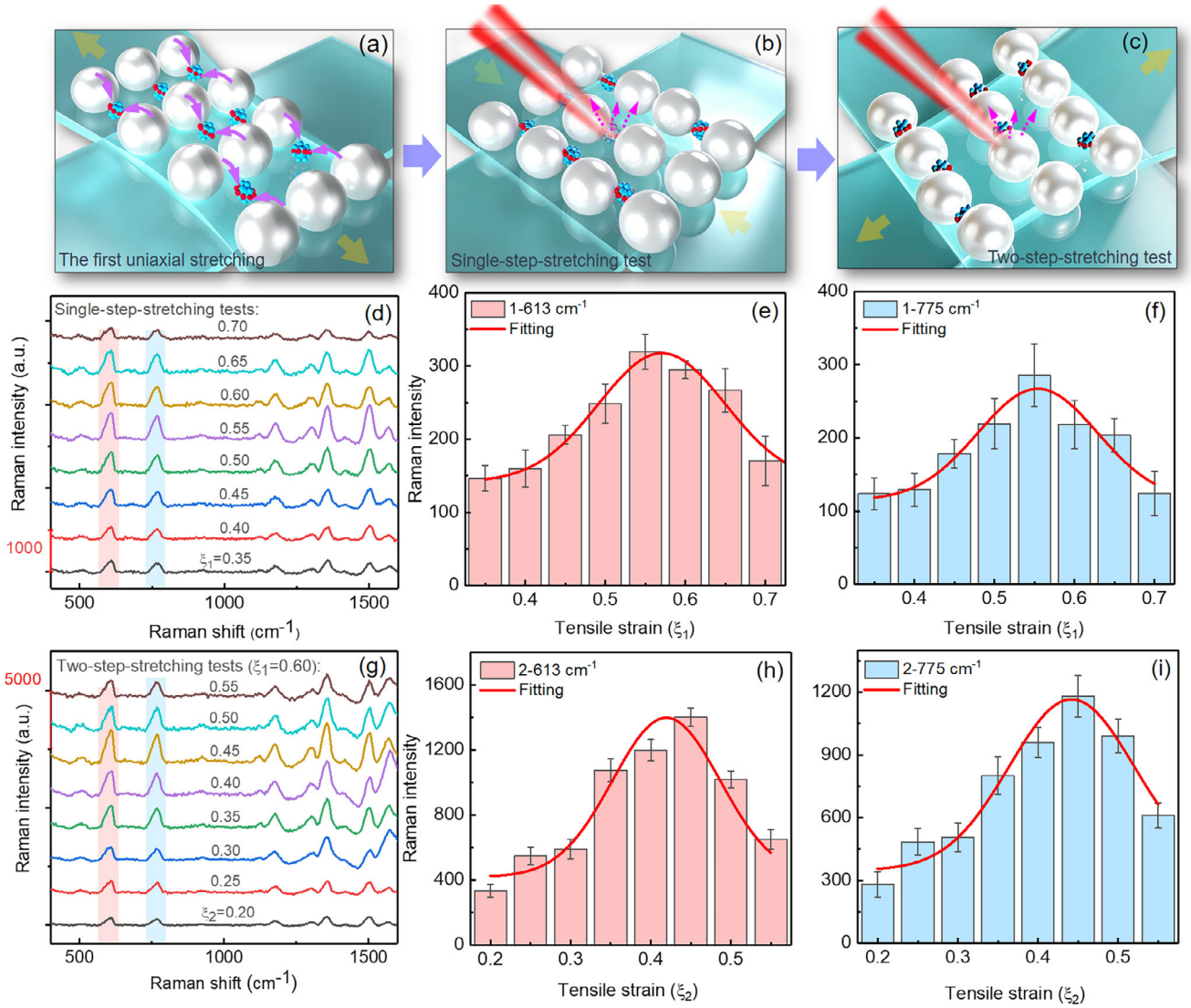


FIGURE 4 | SERS performances of R6G molecules absorbed on the flexible SERS substrates under single uniaxial and two successive orthogonal stretching at different tensile strains. (a)-(c) SERS measurement workflows for the flexible substrates subjected to single uniaxial stretching and two successive orthogonal stretching; (d) SERS spectra of 10^{-7} M R6G molecules collected under single uniaxial stretching; (e) and (f) The intensity evolution of the characteristic peaks as a function of tensile strain ξ_1 at 613 and 775 cm^{-1}, respectively; (g) SERS spectra of 10^{-7} M R6G molecules under two successive orthogonal stretching treatments; (h) and (i) The optimal correlation between the characteristic Raman peak intensity of R6G and the second tensile strain ξ_2 at 613 and 775 cm^{-1}, respectively.

substrate was first stretched to the optimal tensile strain of $\xi_1 = 0.55$, as determined from the aforementioned single-step-stretching measurements, and then followed by the orthogonal stretching with tensile strain ξ_2 varying from 0.2 to 0.55. It has been demonstrated that such a flexible substrate exhibits highly stable SERS performance within 20 stretching cycles. Detailed investigations on substrate stability are presented in Figure S5. In addition to a remarkable improvement in overall SERS intensity, the strain-dependent spectral evolution under orthogonal stretching closely resembles that obtained under single uniaxial stretching. Figure 4h,i summarize the optimal correlation between the characteristic Raman peak intensity of R6G and the second tensile strain ξ_2, which reveals that the maximum SERS signal is stably achieved at $\xi_2 \approx 0.45$. Correspondingly, the calculated SERS EF reaches at least 10^8, which is 5–7-fold higher than that obtained from the single-step stretching test. At high concentrations (e.g., 10^{-7} M R6G), multiple molecules are nearly distributed at every scanned position of the substrate after a single stretch. Therefore, when a second stretch is introduced, the average SERS enhancement mainly originates from the nanogap contraction induced by the two-step stretching strategy and the accompanying enhancement of local electromagnetic fields. By contrast, for low concentrations near the single-molecule regime, the number of molecules residing within hot spots obeys statistical distributions [47–49]. In this case, the second stretch increases the probability of molecules occupying hot spots, leading to a more pronounced enhancement of the overall Raman signal (see experimental investigations below).

With the optimal stretching parameters determined, we systematically investigate and compare the SERS sensitivity or lowest detectable concentration (LDC) of the flexible substrates under

16163028, 0, Downloaded from https://advanced.onlinelibrary.wiley.com/doi/10.1002/adfm.79500 by Fudan University, Wiley Online Library on [10/11/2026]. See the Terms and Conditions (https://onlinelibrary.wiley.com/terms-and-conditions) on Wiley Online Library for rules of use; OA articles are governed by the applicable Creative Commons License

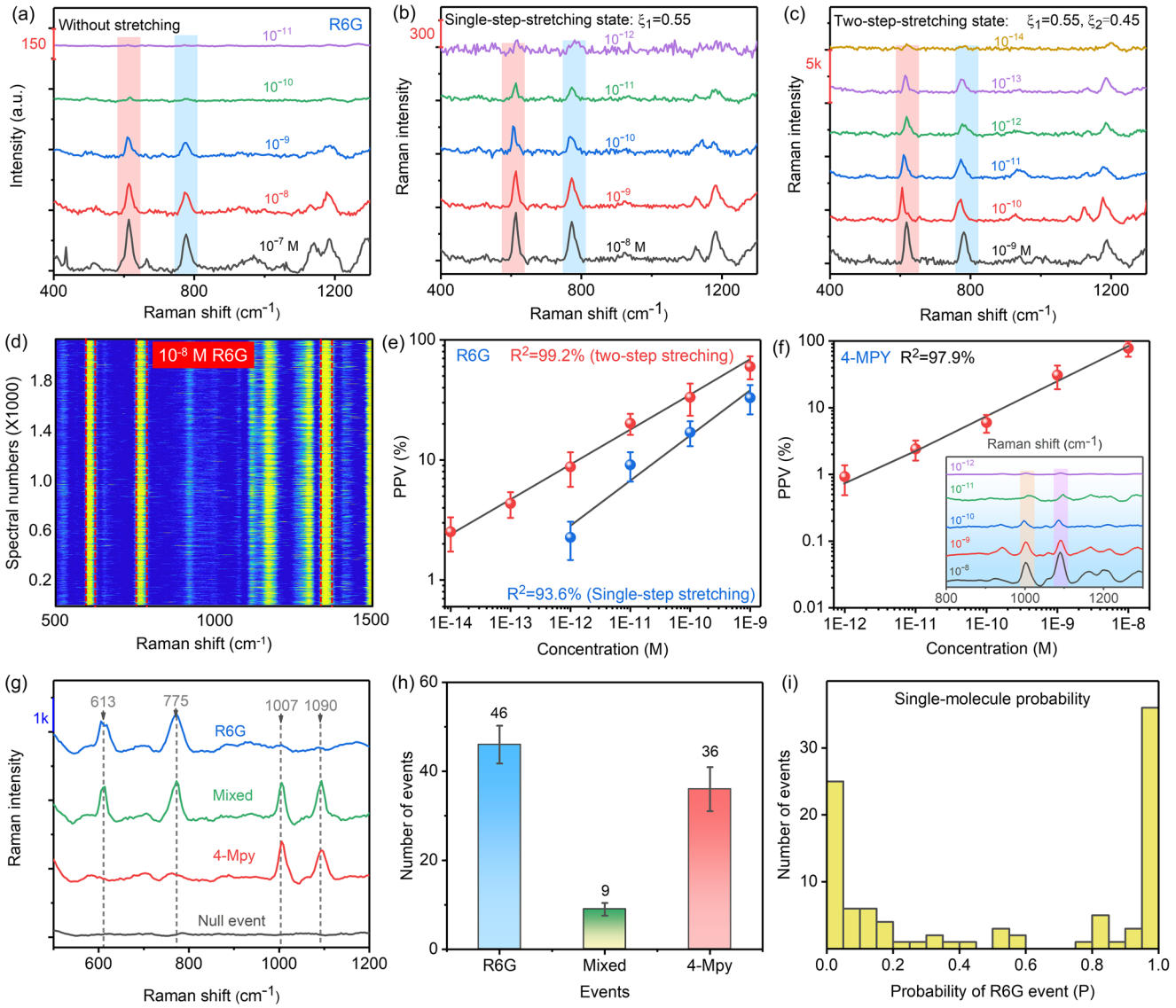


FIGURE 5 | SERS-sensitivity investigation of the flexible SERS substrates under different stretching conditions. (a)-(c) SERS measurement of R6G solutions with different concentrations conducted on flexible substrates under unstretching, single-step-stretching and two-step-stretching conditions, respectively; (d) Spatially scanned measurements of 10^{-8} M R6G solution under two-step-stretching condition; (e) Quantitative correlations between the probability of positive SERS events and molecular concentration for two-step-stretching (red discrete points) and one-step-stretching (blue discrete points) substrates; (f) SERS measurement of 4-MPY solutions conducted on flexible substrate under two-step-stretching condition; (g) Typical bi-analyte spectra corresponding to four different events; (h) Statistical results for the counts of R6G events, 4-MPY events and mixed events; (i) Statistical histogram of the single-molecule frequency derived from MPCA.

unstretched, single-step-stretching, and two-step-stretching conditions. Figure 5a shows the average SERS spectra collected from the unstretched flexible substrate loaded with R6G solution at concentrations ranging from 10^{-7} to 10^{-11} M. As the R6G concentration decreases, its characteristic Raman peaks undergo a corresponding reduction in intensity and can no longer be distinguished at a concentration of 10^{-11} M. Figure 5b,c presents the SERS measurements on the flexible substrate under single-step stretching and two-step stretching conditions, respectively. Compared with the unstretched substrate, flexible SERS substrates under single-step stretching and two-step orthogonal stretching deliver superior SERS enhancement and attain much lower detectable R6G concentrations of 10^{-12} M and 10^{-14} M, respectively. This represents LDC improvements of at least 2 and 4 orders of magnitude, directly demonstrating the effectiveness of mechanical stretching, particularly the two-step strategy, for molecular Raman enhancement.

Figure 5d exhibits the spatially scanned spectra of a 10^{-8} M R6G solution under two-step-stretching conditions, where effective Raman signals of R6G molecules, defined as positive SERS events, are detected at nearly all of the 46 × 46 scanning points. It has been reported recently that the probability of positive SERS events (PPV, P) follows a definite quantitative statistical relation with analyte concentration (C) within the low-concentration regime [47–51]. Derived from the Poisson distribution of target molecular counts within individual detection points, this relation can be formulated as $P = 1 - e^{-a(C)}$, where a denotes the average num-

16163028, 0, Downloaded from https://advanced.onlinelibrary.wiley.com/doi/10.1002/adfm.79500 by Fudan University, Wiley Online Library on [10/11/2026]. See the Terms and Conditions (https://onlinelibrary.wiley.com/terms-and-conditions) on Wiley Online Library for rules of use; OA articles are governed by the applicable Creative Commons License

ber of molecules per detection unit. Under the linear-response approximation valid at sufficiently low concentrations, a scales linearly with C, i.e., $a = \beta C$, where β is a constant incorporating the capture efficiency and detection volume. Therefore, through quantitative statistical analysis of spatially scanned data obtained from R6G solutions with different concentrations (see Figures S6 and S7), we establish a quantitative correlation between the probability of positive SERS events and molecular concentration on a logarithmic scale, as shown in Figure 5e. The criteria for positive SERS events in here are discussed in (see Figure S8). The red discrete points with error bars correspond to the statistical average obtained from three independent measurements on the two-step-stretching substrate; the solid black line denotes the linear fits of the experimental data. The single-stretching data, shown as discrete blue points, are provided for comparison. It should be noted that these three independent experiments represent statistical signals collected from three SERS substrates fabricated in separate batches. The detailed batch-to-batch reproducibility of SERS substrates under different stretching conditions is presented in Figure S9. Well-defined and robust linear correlations between PPV and molecular concentration can be observed over a broad concentration range for both substrates. The coefficient of determination (R^2) reaches approximately 99.2% for the two-step-stretching group, with an average slope of $\beta \approx 0.29$, and 93.6% for the single-step-stretching group, with an average slope of $\beta \approx 0.38$. A comparison between substrates treated with distinct stretching conditions demonstrates clearly that two-step orthogonal stretching substantially improves the number of detectable Raman events, particularly at concentrations approaching the single-molecule detection limit. Meanwhile, this strategy reduces the batch-to-batch relative standard deviation (RSD) of SERS substrates by approximately 5%–10% for a fixed analyte concentration. These findings lay the foundation for highly sensitive and reliable quantitative detection of analytes. Detections of additional analyte molecules further corroborate this conclusion. Figure 5f shows the SERS measurements of 4-MPY solutions at concentrations ranging from 10^{-8} to 10^{-12} M under the two-step-stretched condition. The inset in Figure 5f displays the averaged SERS spectra. Characteristic peaks of 4-MPY can be observed at 1007 and 1090 cm^{-1}, which are consistent with previous reports [27, 52]. Meanwhile, the probability of positive events as a function of 4-MPY molecular concentration exhibits an excellent linear relationship, with R^2 of ~97.9%. Additional SERS measurements for small-molecule analytes (i.e., urea, sodium lactate, and artificial sweat) are provided in Figures S10 and S11. It should be mentioned that the LDC in here is defined based on ratio of the RSD of batch-to-batch measurements on specific molecular concentration to the average probability of positive SERS events $\bar{P}$. We consider that the substrate can reliably resolve molecular concentration features if $RSD/_{\bar{P}} \leq T$, where $T = 30$ is our predefined threshold. Our experiments show that the substrate achieves LDCs for R6G below 10^{-12} M and 10^{-14} M under single and second stretching, respectively, whereas the LDC of 4-MPY upon the second stretch is around 10^{-12} M.

To confirm the single-molecule sensitivity of our system, we perform bi-analyte SERS measurements on the mixed solutions containing 10^{-14} M R6G and 10^{-11} M 4-MPY molecules [53]. Raman peaks at 613/775 cm^{-1}(R6G) and 1007/1090 cm^{-1}(4-MPY) extracted from 1600 scanning spectra are statistically analysed, which are illustrated in Figure S12. Figure 5g presents typical bi-analyte spectra corresponding to four different events. The representative spectra corresponding to the four types of events are shown in Figure S13. In contrast to highly concentrated solutions of the two analytes, which usually generate distinct mixed spectra, the acquired spectra in our measurements are dominated by four cases: signals from a single analyte (R6G event, blue curve, and 4-MPY event, red curve), mixed signals from one R6G molecule together with one 4-MPY molecule (mixed event, green curve), and no detectable signals (null event, black curve). The proportion of R6G events, 4-MPY events, and mixed events is approximately 5:4:1, as depicted in Figure 5h, which agrees with recently reported ratios of single-molecule sensitivity [53–55]. Apart from the rough analysis, we also implement a more rigorous statistical analysis based on modified principal component analysis (MPCA) [54] (see Figure S1). Figure 5i presents the statistical histogram of the single-molecule frequency derived from MPCA. The histogram is dominated by the single-molecule events of $P \approx 1$ (R6G event) and $P \approx 0$ (4-MPY event), which verifies the single-molecule detection regime for our system. The discrepancy in contributions between the $P \approx 1$ and $P \approx 0$ events arises from the distinct Raman scattering cross sections of R6G and 4-MPY molecules [56].

2.3 | Quantitative SERS Detection of Hemoglobin

Using such a high-sensitivity SERS platform, we performed sensor measurements on the large biomolecule hemoglobin (Hb). Hb is a heterotetrameric protein that facilitates the transport of oxygen in red blood cells and possesses a molecular weight of 64 kDa. Figure 6a shows the average SERS spectra of Hb at concentrations ranging from 10 ng/mL to 10 pg/mL, where Hb was dispersed in phosphate buffer solution with a pH of 7.2–7.4. Characteristic peaks of Hb at 764, 1000, 1134, 1304, 1380, and 1455 cm^{-1}, as highlighted by black dotted lines, can be observed, which are basically consistent with recently reported works [35, 57–59]. Although the concentration of the Hb solution decreases to 10 pg/mL, its characteristic Raman peaks can still be clearly resolved. It should be mentioned that the peaks at 1160 cm^{-1} partially overlapping with the Hb characteristic peak at 1134 cm^{-1}, originates from the Raman response of PDMS substrate (see Figure S14). Through double-peak fitting, these overlapping peaks are deconvoluted into the red-filled and blue-filled components, respectively. Figure 6b shows 2D spatial mapping results for 10 pg/mL Hb solution within a 70 μm×70 μm area. The map is plotted based on the characteristic peak at 764 cm^{-1}, which corresponds to the symmetric breathing vibration of the indole ring of tryptophan [57]. Statistical analysis reveals that approximately 120 effective molecular signals were detected among all 4900 scanned points, corresponding to roughly 2.45% of the total scanned sites. By statistically analyzing positive SERS events for Hb solutions of varying concentrations (see Figure 6c), we established a quantitative correlation between PPV and molecular concentration, as illustrated in Figure 6d on a logarithmic scale. The red discrete points with error bars correspond to the statistical average obtained from three repeated measurements of the two-step-stretching substrate, while the blue discrete points are those collected from the one-step-stretching substrate. Obviously, the newly proposed sensing system or sensing strategy exhibits a lower detection limit and more reliable linear quantitative correlations between PPV and

16163028, 0, Downloaded from https://advanced.onlinelibrary.wiley.com/doi/10.1002/adfm.79500 by Fudan University, Wiley Online Library on [10/11/2026]. See the Terms and Conditions (https://onlinelibrary.wiley.com/terms-and-conditions) on Wiley Online Library for rules of use; OA articles are governed by the applicable Creative Commons License

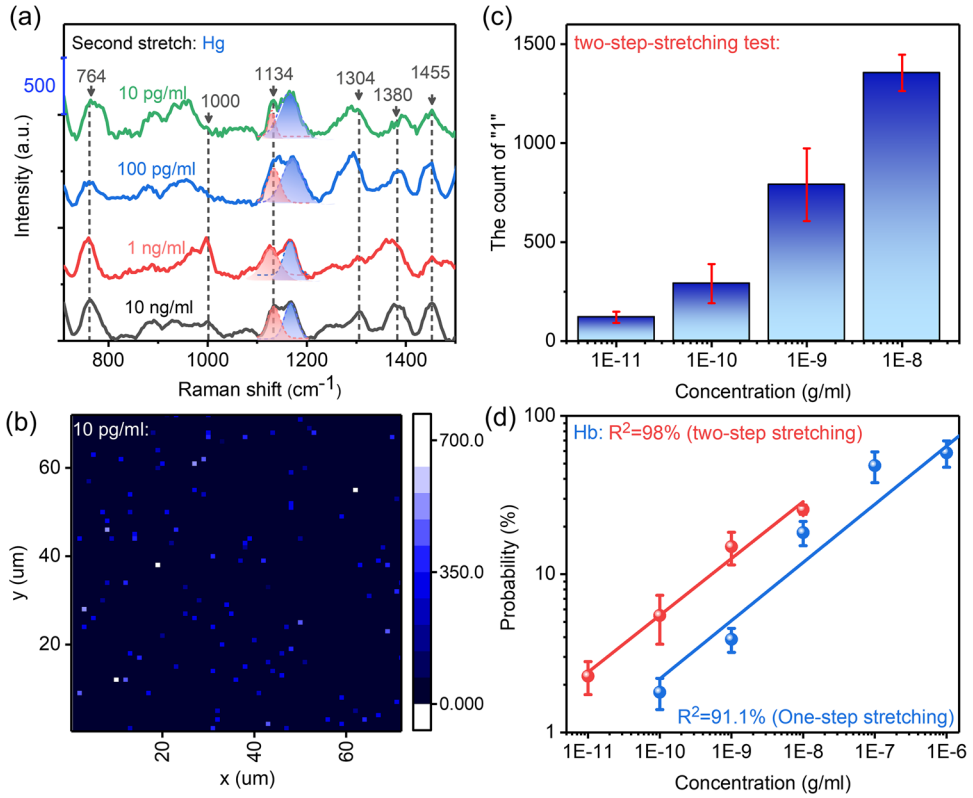


FIGURE 6 | SERS measurements on the biomolecule hemoglobin. (a) SERS spectra of Hb solutions with different concentrations conducted on flexible substrates under two-step-stretching conditions; (b) Spatially scanned measurements for 10 pg/mL Hb solution within a 70 μm×70 μm mapping area; (c) Statistical analysis of positive signal events of Hb solutions with different concentrations; (d) Quantitative correlation between PPV and molecular concentration for two-step-stretching (red discrete points) and one-step-stretching (blue discrete points) substrates.

molecular concentration with $R^2 \approx 98\%$, and with a slope of $\beta \approx 0.358$ (the corresponding 95% confidence interval is [0.232, 0.486]) and. The R^2, slope β, and 95% confidence interval obtained from the linear fitting of the single-stretching measurement are about 91%, 0.359 and [0.227, 0.49], respectively. Overall, sensing measurements on the above diverse molecules fully demonstrate the excellent versatility and reliable quantitative-detection capability of this system. A detailed performance comparison between this work and previous studies on tunable nanogaps is presented in Table S1.

3 | Conclusions

In this study, we propose a stepwise plasmonic nanogap modulation strategy that enables sequential regulation of nanogap expansion and contraction on stretchable substrates decorated with randomly distributed silver nanoparticles. This strategy features high efficiency, superior precision, facile operation, and low fabrication cost. More importantly, the versatile tunability of plasmonic nanogaps greatly facilitates the trapping and deposition of analyte molecules and sequential SERS enhancement. Such favorable performances are well validated by SERS intensity responses from analytes as well as the statistical proportion of positive SERS events obtained via scanning measurements. Furthermore, SERS tests on diverse targets, including small molecules (R6G, 4-MPY, urea, and sodium lactate), large biomolecules (Hb), and dual-analyte mixtures, distinctly demonstrate the high sensitivity, excellent reconfigurability, and reliable quantitative-detection capability of the developed SERS sensing platform.

4 | Methods

4.1 | Fabrication of the SERS Substrate

The flexible substrate was first trimmed into a cross-shaped geometry to facilitate subsequent two-step orthogonal stretching. The pre-processed substrate was ultrasonically cleaned in an alcohol solution for 30 min to remove surface contaminants, and then transferred to a thermal evaporation system. After 2 h of vacuum pumping, silver was thermally evaporated onto the substrate surface at an average deposition rate of 0.1 Å/s. Benefiting from the intrinsic micro-nano roughness of the substrate, a uniform and randomly distributed monolayer of Ag nanoparticles was successfully fabricated after 15–20 min of evaporation.

4.2 | Optical Spectroscopic Characterizations

The flexible SERS substrate was mounted on a stretchable translation stage (see Figure S2), which was integrated into a home-made transmission/reflection spectral measurement system. A supercontinuum white-light laser was utilized as the incident light source in this setup. The incident beam passed through a polarizer and then irradiated normally onto the surface

16163028, 0, Downloaded from https://advanced.onlinelibrary.wiley.com/doi/10.1002/adfm.79500 by Fudan University, Wiley Online Library on [10/11/2026]. See the Terms and Conditions (https://onlinelibrary.wiley.com/terms-and-conditions) on Wiley Online Library for rules of use; OA articles are governed by the applicable Creative Commons License

of the flexible SERS substrate, where either TE or TM polarization can be chosen during the measurements. A fiber spectrometer was employed to collect the transmission and reflection spectra of the substrate. Finally, the absorption spectra of the substrate under different stretching strains were quantitatively calculated according to the formula of $A = 1 - T - R$, where A, T and R denote the absorption, transmission, and reflection spectra, respectively.

4.3 | Numerical Simulations

Simulations of optical absorption spectra and electric field intensity distribution were performed using Finite-Difference Time-Domain (FDTD) software, in which the 3D Mie scattering mode was adopted. Correspondingly, perfectly matched layer (PML) boundary conditions were applied to all four boundaries. The Total Field Scattered Field (TFSF) source was placed between the scattering and absorption monitors, maintaining a gap of at least two mesh cells between the TFSF boundary and the Ag nanoparticles. A minimum mesh cell size of 1 nm was used. The optical constants of silver were taken from Ref. [60], and the entire structure was surrounded by a homogeneous medium with a refractive index of $n = 1$.

4.4 | SERS Measurements

After the flexible SERS substrate was pre-stretched to a certain length, approximately 2 μL analyte solution was drop-cast onto its surface. The sample was left to dry completely for about 30 min before subsequent SERS measurements. A reflective confocal Raman microscope with an excitation laser at $\lambda_{exc} = 532$ nm (through a 100× objective lens) was applied with a beam spot size of 800 nm in diameter. The Raman spectra were recorded from an upright-configured confocal microscope equipped with an iHR320 CCD detector. The laser output power was maintained at about 0.15 mW for all measurements. Moreover, during SERS tests upon secondary stretching, the polarization of the excitation light was maintained perpendicular to the substrate-stretching direction. The integration time for SERS spectra and the number of accumulations per spectrum were fixed at 1 s and 1, respectively.

Rather than making the standard assumption that Raman scattering arises only from a monolayer of molecules that cover the effective surface of the nanostructures, we here employ a measure defined by the averaged enhancement factor that originates from all molecules in the system:

$$\overline{EF} = \frac{I}{I_0}\frac{C_0}{C}\frac{P_0}{P}$$

where I is the Raman intensity, C is the concentration of the molecular solution, P is the laser power. I_0, C_0, and P_0 are the corresponding values for the reference substrate, such as a pure Ag film.

Author Contributions

Jiaye Du: investigation, validation, data curation, formal analysis. **Ruirui Ren**: investigation, methodology, data curation. **Fengguang Shen**: investigation, validation. **Jiajun Li**: methodology, formal analysis. **Leilei Hou**: methodology, software. **Jingjing Wei**: investigation. **Xiuying Liu**: formal analysis, funding acquisition. **Ming Kang**: supervision, formal analysis. **Lei Zhou**: writing – review and editing, project administration, funding acquisition, conceptualization. **Feifei Liu**: conceptualization, methodology, funding acquisition, project administration, writing – original draft, writing – review and editing, formal analysis.

Acknowledgements

This work was supported by the National Natural Science Foundation of China (Grant Nos. 62005197, 12204349, 12221004 and 62192771), the National Key Research and Development Program of China (Grant No. 2022YFA1404700), the open project from State Key Laboratory of Surface Physics at Fudan University (Grant No. KF202513), the open project from Tianjin Key Laboratory of Low-Dimensional Electronic Materials and Advanced Instrumentation (Grant No. TKL-KF-2025-01), Tianjin Normal University's Graduate Innovation Project (No. YZ018243003 and YZ018253002) and the Natural Science Foundation of Shanghai (Grant No. 23dz2260100).

Conflicts of Interest

The authors declare no conflicts of interest.

Data Availability Statement

The data that support the findings of this study are available from the corresponding author upon reasonable request.

References

1. A. Campion and P. Kambhampati, "Surface-Enhanced Raman Scattering," *Chemical Society Reviews* 27 (1998): 241–250, https://doi.org/10.1039/a827241z.

2. H. L. Wang, E. M. You, R. Panneerselvam, S. Y. Ding, and Z. Q. Tian, "Advances of Surface-Enhanced Raman and IR Spectroscopies: From Nano/Microstructures to Macro-Optical Design," *Light: Science Applied* 10 (2021): 161, https://doi.org/10.1038/s41377-021-00599-2.

3. A. I. Perez-Jimenez, D. Y. Lyu, and Z. X. Lu, "Surface-Enhanced Raman Spectroscopy: Benefits, Trade-Offs and Future Developments," *Chemical Science* 11 (2020): 4563–4577.

4. Y. Xu, W. Aljuhani, Y. Zhang, Z. Ye, C. Li, and S. E. J. Bell, "A Practical Approach to Quantitative Analytical Surface-Enhanced Raman Spectroscopy," *Chemical Society Reviews* 54 (2025): 62–84, https://doi.org/10.1039/D4CS00861H.

5. Y. Fang, N. H. Seong, and D. D. Dlott, "Measurement of the Distribution of Site Enhancements in Surface-Enhanced Raman Scattering," *Science* 321 (2008): 388–392.

6. E. Hutter and J. H. Fendler, "Exploitation of Localized Surface Plasmon Resonance," *Advanced Materials* 16 (2004): 1685–1706, https://doi.org/10.1002/adma.200400271.

7. K. A. Willets and R. P. Van Duyne, "Localized Surface Plasmon Resonance Spectroscopy and Sensing," *Annual Review of Physical Chemistry* 58 (2007): 267–297, https://doi.org/10.1146/annurev.physchem.58.032806.104607.

8. H. X. Xu, E. J. Bjerneld, M. Kall, and L. Borjesson, "Spectroscopy of Single Hemoglobin Molecules by Surface Enhanced Raman Scattering," *Physical Review Letters* 83 (1999): 4357–4360, https://doi.org/10.1103/PhysRevLett.83.4357.

9. Y. Li, W. Chen, X. He, et al., "Boosting Light-Matter Interactions in Plasmonic Nanogaps," *Advanced Materials* 36 (2024): 2405186.

10. X. L. Miao, L. Y. Yan, Y. Wu, and P. Q. Liu, "High-Sensitivity Nanophotonic Sensors With Passive Trapping of Analyte Molecules in Hot Spots," *Light: Science & Applications* 10 (2021): 5, https://doi.org/10.1038/s41377-020-00449-7.

16163028, 0, Downloaded from https://advanced.onlinelibrary.wiley.com/doi/10.1002/adfm.79500 by Fudan University, Wiley Online Library on [10/11/2026]. See the Terms and Conditions (https://onlinelibrary.wiley.com/terms-and-conditions) on Wiley Online Library for rules of use; OA articles are governed by the applicable Creative Commons License

11. M. H. Ge, P. Li, G. L. Zhou, et al., "General Surface-Enhanced Raman Spectroscopy Method for Actively Capturing Target Molecules in Small Gaps," *Journal of the American Chemical Society* 143 (2021): 7769–7776, https://doi.org/10.1021/jacs.1c02169.

12. P. Zheng, L. Wu, P. Raj, et al., "Multiplexed SERS Detection of Serum Cardiac Markers Using Plasmonic Metasurfaces," *Advanced Science* 11 (2024): 2405910.

13. M. Hao, S. Q. Pan, W. L. Wang, et al., "Surface-Enhanced Raman Spectroscopy: Current Understanding, Challenges, and Opportunities," *ACS Nano* 18 (2024): 14000–14019.

14. G. H. Kim, J. Son, and J. M. Nam, "Advances, Challenges, and Opportunities in Plasmonic Nanogap-Enhanced Raman Scattering With Nanoparticles," *ACS Nano* 19 (2025): 2992–3007, https://doi.org/10.1021/acsnano.4c14557.

15. S. Sloan-Dennison, G. Q. Wallace, W. A. Hassanain, S. Laing, K. Faulds, and D. Graham, "Advancing SERS as a Quantitative Technique: Challenges, Considerations, and Correlative Approaches to Aid Validation," *Nano Converg* 11 (2024): 33, https://doi.org/10.1186/s40580-024-00443-4.

16. M. K. Fan and A. G. Brolo, "Factors That Affect Quantification in Surface-Enhanced Raman Scattering," *ACS Nano* 19 (2025): 3969–3996, https://doi.org/10.1021/acsnano.4c15183.

17. S. Yan, H. Tang, L. Wen, N. Wu, and G. Meng, "Crucial Factors for Reproducible and Ultrasensitive Surface-Enhanced Raman Spectroscopy Detection: Hot Spot Engineering and Molecular Delivery," *Advanced Optical Materials* 14, no. 12 (2026): e02275.

18. Q. Feng, X. H. Liu, H. Liu, C. Liu, H. Jiang, and X. M. Wang, "Metal-Based Flexible Optoelectronic Materials: From Structural Foundation to Biomedical Sensor Application," *Advanced Optical Materials* 13 (2025): 20240467, https://doi.org/10.1002/adom.202502404.

19. R. Peng, T. T. Zhang, S. Yan, Y. X. Song, X. Y. Liu, and J. S. Wang, "Recent Development and Applications of Stretchable SERS Substrates," *Nanomaterials* 13, no. 22 (2023): 2968.

20. L. P. Xie, H. D. Zeng, J. X. Zhu, et al., "State of the Art in Flexible SERS Sensors Toward Label-Free and Onsite Detection: From Design to Applications," *Nano Research* 15 (2022): 4374–4394.

21. K. Xu, R. Zhou, K. Takei, and M. Hong, "Toward Flexible Surface-Enhanced Raman Scattering (SERS) Sensors for Point-of-Care Diagnostics," *Advanced Science* 6, no. 16 (2019): 1900925.

22. Y. Wang, C. Zhao, J. Wang, et al., "Wearable Plasmonic-Metasurface Sensor for Noninvasive and Universal Molecular Fingerprint Detection on Biointerfaces," *Science Advances* 7 (2021): abe4553, https://doi.org/10.4028/b-dOXV17.

23. F. Laible, A. Horneber, and M. Fleischer, "Mechanically Tunable Nanogap Antennas: Single-Structure Effects and Multi-Structure Applications," *Advanced Optical Materials* 9 (2021): 2100326.

24. Z. Wang, K. W. Li, N. Zhang, et al., "Formation of Ultra-Flexible, Conformal, and Nano-Patterned Photonic Surfaces via Polymer Cold-Drawing," *Journal of Materials Chemistry C* 6 (2018): 4649–4657.

25. M. H. Moghaddam, S. Sharma, D. Park, and D. S. Kim, "Tuning 1D Plasmonic Gap at Nanometer Scale for Advanced SERS Detection," *Advanced Optical Materials* 13, no. 11 (2025): 2403021.

26. H. Mitomo, K. Horie, Y. Matsuo, et al., "Active Gap SERS for the Sensitive Detection of Biomacromolecules With Plasmonic Nanostructures on Hydrogels," *Advanced Optical Materials* 4 (2016): 259–263, https://doi.org/10.1002/adom.201500509.

27. H. Xiang, X. Yang, Z. Liu, et al., "Wearable Optical Fiber SERS Sensor Based on a Flexible "Hydrogel Tentacle" for Sweat Remote and *in Situ* Detection," *ACS Sensors* 11 (2026): 2625–2635.

28. V. Eskandari, H. Sahbafar, L. Zeinalizad, R. Marashipour, and A. Hadi, "A Review of Paper-Based Substrates as Surface-Enhanced Raman Spectroscopy (SERS) Biosensors and Microfluidic Paper-Based SERS Platforms," *Journal of Computational Applied Mechanics* 53 (2022): 142–156.

29. U. Cataldi, R. Caputo, Y. Kurylyak, et al., "Growing Gold Nanoparticles on a Flexible Substrate to Enable Simple Mechanical Control of Their Plasmonic Coupling," *Journal of Materials Chemistry C* 2 (2014): 7927–7933, https://doi.org/10.1039/C4TC01607F.

30. R. V. Carréon, A. G. Rodríguez-Hernández, L. E. S. Rosa, J. J. Gervacio-Arciniega, and S. K. M. F. Krishnan, "Mechanically Flexible, Large-Area Fabrication of Three-Dimensional Dendritic Au Films for Reproducible Surface-Enhanced Raman Scattering Detection of Nanoplastics," *ACS Sensors* 10 (2025): 1747–1755, https://doi.org/10.1021/acssensors.4c02081.

31. T. Moon, H. Joo, B. Das, et al., "Adaptive Gap-Tunable Surface-Enhanced Raman Spectroscopy," *Nano Letters* 24 (2024): 3777–3784, https://doi.org/10.1021/acs.nanolett.4c00289.

32. H. Kang, C.-J. Heo, H. C. Jeon, S. Y. Lee, and S.-M. Yang, "Durable Plasmonic Cap Arrays on Flexible Substrate With Real-Time Optical Tunability for High-Fidelity SERS Devices," *ACS Applied Materials & Interfaces* 5 (2013): 4569–4574, https://doi.org/10.1021/am400019v.

33. Q. Q. Ding, X. Y. Chen, Y. L. Jia, et al., "Timeshare Surface-Enhanced Raman Scattering Platform With Sensitive and Quantitative Mode," *Optoelectronics and Advanced Materials* 9 (2026): 250269.

34. G. Li, X. Zhao, X. Tang, et al., "Wearable Hydrogel SERS Chip Utilizing Plasmonic Trimers for Uric Acid Analysis in Sweat," *Nano Letters* 24 (2024): 13447–13454, https://doi.org/10.1021/acs.nanolett.4c04267.

35. T. Gao, T. Yachi, X. Shi, et al., "Ultrasensitive Surface-Enhanced Raman Scattering Platform for Protein Detection via Active Delivery to Nanogaps as a Hotspot," *ACS Nano* 18 (2024): 21593–21606, https://doi.org/10.1021/acsnano.4c09578.

36. Y. Mu and X. Zhang, "A Paper-Fiber-Supported 3D SERS Substrate," *Plasmonics* 15 (2020): 889–896, https://doi.org/10.1007/s11468-019-01097-3.

37. Y. Wu, T. Sun, Z. Pei, et al., "Light-Field and External-Field Modulation in Surface-Enhanced Raman Scattering: Strategies and Prospects," *Light Manipulation and Applications* 1 (2026): 202601.

38. Z. Pei, C. Ji, M. Shao, et al., "Enrichment Strategies in Surface-Enhanced Raman Scattering: Theoretical Insights and Optical Design for Enhanced Light-Matter Interaction," *OptoElectronic Science* 4 (2025): 250015.

39. Q. Y. Lin, Z. Y. Li, K. A. Brown, et al., "Strong Coupling Between Plasmonic Gap Modes and Photonic Lattice Modes in DNA-Assembled Gold Nanocube Arrays," *Nano Letters* 15 (2015): 4699–4703, https://doi.org/10.1021/acs.nanolett.5b01548.

40. F. Liu, X. Zhang, and X. Fang, "Plasmonic Plano-Semi-Cylindrical Nanocavities With High-Efficiency Local-Field Confinement," *Scientific Reports* 7 (2017): 40071.

41. F. Liu, J. Wei, H. Jia, et al., "Meta-Grating-Based SERS Sensor Capable of Efficiently Trapping Target Molecules in Hotspots," *Applied Physics Letters* 128 (2026): 251702.

42. H. H. Li, J. Z. Zhang, Z. H. Gao, et al., "Counting, Identifying, and Distinguishing Single Molecules from Their Mixtures via Raman Spectroscopy," *Nano Letters* 25 (2025): 12947–12953.

43. N. Gao, L. Wang, X. Li, et al., "Reconfigurable SERS Platform Based on Magnetization-Controlled Self-Assembly of Magnetic Nanoparticles on NdFeB Composite Substrate," *Optoelectronics and Advanced Materials* 9 (2026): 260135.

44. S. Deng, W. Dou, Y. Wu, et al., "Dual-Tunable SERS Substrate: Synergistic Enhancement via Plasmonic Resonance Tailoring and Pyroelectric Field Modulation in Ag/BTO Hybrid Arrays," *Optics & Laser Technology* 203 (2026): 115468.

45. S. Y. Ding, E. M. You, Z. Q. Tian, and M. Moskovits, "Electromagnetic Theories of Surface-Enhanced Raman Spectroscopy," *Chemical Society Reviews* 46 (2017): 4042–4076, https://doi.org/10.1039/C7CS00238F.

46. Y. Yu, T. H. Xiao, Y. Z. Wu, et al., "Roadmap for Single-Molecule Surface-Enhanced Raman Spectroscopy," *Advances Photonics* 2 (2020): 014002.

16163028, 0, Downloaded from https://advanced.onlinelibrary.wiley.com/doi/10.1002/adfm.79500 by Fudan University, Wiley Online Library on [10/11/2026]. See the Terms and Conditions (https://onlinelibrary.wiley.com/terms-and-conditions) on Wiley Online Library for rules of use; OA articles are governed by the applicable Creative Commons License

47. C. D. L. de Albuquerque, R. G. Sobral-Filho, R. J. Poppi, and A. G. Brolo, "Digital Protocol for Chemical Analysis at Ultralow Concentrations by Surface-Enhanced Raman Scattering," *Analytical Chemistry* 90 (2018): 1248–1254.

48. X. Y. Bi, D. M. Czajkowsky, Z. F. Shao, and J. Ye, "Digital Colloid-Enhanced Raman Spectroscopy by Single-Molecule Counting," *Nature* 628 (2024): 771–790.

49. H. Zhang, L. Yang, M. Zhang, et al., "A Statistical Route to Robust SERS Quantitation Beyond the Single-Molecule Level," *Nano Letters* 24 (2024): 11116–11123, https://doi.org/10.1021/acs.nanolett.4c03507.

50. W. Yang, M. M. Liang, G. Y. Sun, et al., "Statistical Strategy for Quantitative Evaluation of Plasmon-Enhanced Spectroscopy," *ACS Photonics* 9 (2022): 1733–1740.

51. P. Wen, F. Yang, H. Zhao, S. Li, Y. Xu, and L. Chen, "Microcavity Array-Based Digital SERS Chip for Rapid and Accurate Label-Free Quantitative Detection of Live Bacteria," *ACS Sensors* 9 (2024): 6167–6173, https://doi.org/10.1021/acssensors.4c02007.

52. J. S. Figueiredo, S. Fateixa, J. D. Gouveia, J. R. B. Gomes, and T. Trindade, "Insights on Charge-Transfer Mechanisms in ZnO and ZnO–GO Substrates for the SERS Analysis of 4-Mercaptopyridine," *The Journal of Physical Chemistry C* 130 (2026): 10618–10630, https://doi.org/10.1021/acs.jpcc.6c01798.

53. E. C. Le Ru, M. Meyer, and P. G. Etchegoin, "Proof of Single-Molecule Sensitivity in Surface-Enhanced Raman Scattering (SERS) by Means of a Two-Analyte Technique," *Journal of Physical Chemistry B* 110 (2006): 1944–1948.

54. P. Mao, C. Liu, G. Favraud, et al., "Broadband Single Molecule SERS Detection Designed by Warped Optical Spaces," *Nature Communications* 9 (2018): 5428.

55. Q. Hao, Z. H. Peng, J. W. Wang, et al., "Verification and Analysis of Single-Molecule SERS Events via Polarization-Selective Raman Measurement," *Analytical Chemistry* 94 (2022): 1046–1051, https://doi.org/10.1021/acs.analchem.1c04015.

56. X. Zhao, X. Liu, D. Chen, et al., "Plasmonic Trimers Designed as SERS-Active Chemical Traps for Subtyping of Lung Tumors," *Nature Communications* 15 (2024): 5855.

57. D. Drescher, T. Büchner, D. McNaughton, and J. Kneipp, "SERS Reveals the Specific Interaction of Silver and Gold Nanoparticles With Hemoglobin and Red Blood Cell Components," *Physical Chemistry Chemical Physics* 15 (2013): 5364–5373, https://doi.org/10.1039/c3cp43883j.

58. P. Lemler, W. R. Premasiri, A. DelMonaco, and L. D. Ziegler, "NIR Raman Spectra of Whole Human Blood: Effects of Laser-Induced and *in Vitro* Hemoglobin Denaturation," *Analytical and Bioanalytical Chemistry* 406 (2014): 193–200, https://doi.org/10.1007/s00216-013-7427-7.

59. A. Das, U. Pant, C. Cao, R. S. Moirangthem, and H. B. Kamble, "Fabrication of Plasmonic Nanopyramidal Array as Flexible SERS Substrate for Biosensing Application," *Nano Research* 16 (2023): 1132–1140, https://doi.org/10.1007/s12274-022-4745-0.

60. P. B. Johnson and R. W. Christy, "Optical Constants of the Noble Metals," *Physical Review B* 6 (1972): 4370–4379, https://doi.org/10.1103/PhysRevB.6.4370.

Supporting Information

Additional supporting information can be found online in the Supporting Information section.

Supporting File: adfm79500-sup-0001-SuppMat.docx.

16163028, 0, Downloaded from https://advanced.onlinelibrary.wiley.com/doi/10.1002/adfm.79500 by Fudan University, Wiley Online Library on [10/11/2026]. See the Terms and Conditions (https://onlinelibrary.wiley.com/terms-and-conditions) on Wiley Online Library for rules of use; OA articles are governed by the applicable Creative Commons License